The Astrophysical Journal Letters, 1000:L21 (6pp), 2026 March 20 https://doi.org/10.3847/2041-8213/ae4c52

Toward Black Hole Stars: Supermassive Black Hole Growth in Nuclear Clusters via Stellar-object and Gas Accretion

Konstantinos Kritos[1] and Joseph Silk[1,2,3]
[1] William H. Miller III Department of Physics and Astronomy, Johns Hopkins University, 3400 North Charles Street, Baltimore, MD 21218, USA; kkritos1@jhu.edu
[2] Institut d'Astrophysique de Paris, UMR 7095 CNRS and UPMC, Sorbonne Université, F-75014 Paris, France
[3] Department of Physics, Beecroft Institute for Particle Astrophysics and Cosmology, University of Oxford, Oxford OX1 3RH, UK
Received 2026 February 5; revised 2026 February 25; accepted 2026 February 26; published 2026 March 16

Abstract

Supermassive black hole (SMBH) growth plausibly occurs via runaway astrophysical black hole mergers in nuclear star clusters that form intermediate mass black hole seeds at high redshifts. Such a model yields an order-of-magnitude higher rate of tidal disruption events than that of compact-object captures. Our prediction, normalized to our proposed resolution of SMBH seeding, yields detectable tidal disruption event rates at high redshift. The resulting dense gas cocoons generate compact galactic nuclei, each incorporating a central, massive, black hole star, with comparable masses in gas, stars, and massive black holes within a scale of around a parsec as inferred from the various Little Red Dot spectral signatures.

Unified Astronomy Thesaurus concepts: Stellar dynamics (1596); Gravitational wave sources (677); Transient sources (1851)

1. Introduction

Extreme nuclear transients (ENTs) are rare, ultraluminous flares ($>10^{45}$ erg s^{-1}), exceeding supernova energies and more easily detected at $z > 1$ than classical tidal disruption events (TDEs) in flux-limited surveys. The JWST has also uncovered numerous "Little Red Dots" (LRDs; $4 < z < 8$), likely AGN powered by $\sim 10^7$–$10^8\,M_\odot$ supermassive black holes (SMBHs; J. E. Greene et al. 2024; R. Maiolino et al. 2024; J. Matthee et al. 2024).

ENTs show slow decays ($\gtrsim$150 days), emit more total energy than TDEs, and have smooth (<10% variability) light curves, blue spectra, and broad lines distinguishing them from AGN variability or supernovae (S. Frederick et al. 2021). They are proposed to be TDEs of high-mass stars ($>3\,M_\odot$) by SMBHs (J. T. Hinkle et al. 2025).

Typical TDE durations are 3×10^6–10^7 s (D. Melchor et al. 2025). Rates are $\sim 10^{-5}$ galaxy^{-1} yr^{-1} in normal galaxies, enhanced by 10–100 times in poststarburst systems (S. van Velzen et al. 2020). A new class of ambiguous nuclear transients (ANTs) is also observed (P. Wiseman et al. 2025).

J. Bellovary (2025) estimates a high-z TDE rate of $\sim 10^{-4}$ yr^{-1} (for $5 < z < 8$) by linking LRDs to SMBH-seed densities assuming purely TDE-powered emission, a rate too low for SMBH growth and implying LRD masses below earlier claims. A $\sim 10^7\,M_\odot$ black hole (BH) has meanwhile been directly measured in a lensed $z = 7$ LRD (I. Juodžbalis et al. 2025). Since LRDs are likely AGN-dominated, K. Kritos & J. Silk (2025) show that including SMBH-growth needs (mergers + accretion) significantly boosts high-z TDE rates, which we argue here may be observable.

In this work, we analyze an N-body snapshot at time t of a star cluster within a central SMBH's sphere of influence by sampling its spherically symmetric distribution function without time evolution. From these snapshots, we compute the instantaneous TDE and compact-object capture rates, incorporating loss-cone physics and stellar evolution.

2. Stellar Feeding onto Central Hole

We model a nuclear star cluster (NSC) around an SMBH of mass $M_{\rm SMBH}$ and dimensionless spin parameter $a_{\rm SMBH}$. A star of mass $m_\star$ and radius $R_\star$ is removed if its pericenter lies within the loss-cone radius $r_{\rm lc} = \max(r_{\rm T}, r_{\rm mb})$, where $r_{\rm T} = R_\star (M_{\rm SMBH}/m_\star)^{1/3}$ (C. R. Evans & C. S. Kochanek 1989) and $r_{\rm mb}$ is the spin-dependent marginally bound orbit. For $r_{\rm T} \gtrsim r_{\rm mb}$, the event produces an electromagnetic TDE (A. Mummery 2024). Stars enter the loss cone via relaxation and are removed on a crossing time.

We compute event rates with Monte Carlo simulations in the Keplerian potential $\Phi = -GM_{\rm SMBH}/r$ within the influence radius $r_{\rm infl}$, containing $N_\star \simeq 2M_{\rm SMBH}/\overline{m}_\star$ stars. Stellar masses are drawn from an initial mass function (IMF) and evolved with `updated-BSE` (S. Banerjee et al. 2020). Assuming $n_\star \propto r^{-\gamma}$ we sample radii from $p(r) \propto r^{3-\gamma}$ and orbits from the isotropic distribution $f(a,\, e) \propto a^{2-\gamma} e$ (D. Merritt 2013, Equation (4.36)). Orbital periods follow from Kepler's law, $P \simeq 2\pi G M_{\rm SMBH} m_\star (-E)^{-3/2}$.

Angular-momentum diffusion is driven by nonresonant relaxation (NRR) with a timescale (D. Merritt 2013, Equation (5.61))

$$t_{\rm NRR} \simeq \frac{1.8\ {\rm Gyr}}{\ln\Lambda} \frac{10^7\,M_\odot\ {\rm pc}^{-3}}{\rho_\star} \times \frac{1\,M_\odot}{m} \left(\frac{\sigma_\star}{100\ {\rm km\ s}^{-1}} \right)^3, \quad (1)$$

where $\sigma_\star = (1+\gamma)^{-1/2} (GM_{\rm SMBH}/r)^{1/2}$ and $\ln\Lambda \simeq \ln N_\star$. In the Keplerian regime, we also include resonant relaxation (RR; K. P. Rauch & S. Tremaine 1996; M. A. Gurkan & C. Hopman2007), with an effective relaxation time $t_{\rm R} = (t_{\rm NRR}^{-1} + t_{\rm RR}^{-1})^{-1}$ (C. Hopman & T. Alexander 2006a, Equation (11)).

Feeding rates are computed using the loss-cone theory by D. Syer & A. Ulmer (1999). Defining $\theta_{\rm D} = (P/t_{\rm R})^{1/2}$ (J. Frank & M. J. Rees 1976, Equation (12)), the loss cone is empty for $\theta_{\rm lc} > \theta_{\rm D}$, with rate $[\ln(2/\theta_{\rm lc})t_{\rm R}]^{-1}$, and full otherwise, with rate $\theta_{\rm lc}^2/P$ per unit star. Summing over stars within $r_{\rm infl}$ yields the total instantaneous rate $\Gamma_{\rm lc}(t|M_{\rm SMBH})$.

For compact objects, we additionally include capture by gravitational bremsstrahlung (G. D. Quinlan & S. L. Shapiro 1989, Equation (11)) and gravitational wave (GW)-driven inspirals, known as extreme mass-ratio inspirals (EMRIs). The effective loss-cone radius is the maximum of tidal, bremsstrahlung, and marginally bound radii. For EMRIs, $\theta_{\rm D} = (t_{\rm GW}/t_{\rm R})^{1/2}$ and the full-loss-cone regime is absent (T. Alexander & C. Hopman 2003). We compute $t_{\rm GW}$ using the fit of I. Mandel (2021).

3. Initial Conditions

We adopt a canonical IMF spanning 0.08–150 $M_\odot$ at metallicity $Z = 0.002$. Stellar types from `updated-BSE` are grouped into stellar classes indexed by A as "main sequence (MS)" (1–2), "giants" (3–6), "cores" (7–9), "white dwarfs (WDs)" (10–12), "neutron stars (NSs)" (13), and "BHs" (14).

Orbits are initialized with a thermal eccentricity distribution; departures from thermal (e.g., superthermal) enhance captures and inspirals by increasing the low-angular-momentum population.

We assume approximate energy equipartition within $r_{\rm infl}$, leading to mass segregation (C. Hopman & T. Alexander 2006b). Stars, WDs, and NSs follow density slopes $\gamma_\star = 1.5$, while stellar-mass BHs are more centrally concentrated with $\gamma_{\rm BH} = 2$.

Five representative time epochs (10^0, 10^1, 10^2, 10^3, and 10^4 Myr) and three SMBH masses (10^5, 10^6, and $10^7\,M_\odot$) are considered with $a_{\rm SMBH} = 0.5$. We link $r_{\rm infl} = GM_{\rm SMBH}/\sigma^2$ to $M_{\rm SMBH}$ through the $M_{\rm SMBH}$–σ relation (N. J. McConnell et al. 2011, Figure 3). We assume the SMBH influence region is fully populated ($M_\star \gtrsim M_{\rm SMBH}$); otherwise, rates would scale down accordingly.

4. Mass Accretion Rate

Figure 1 shows the SMBH mass accretion rate by stellar type. Means and standard deviations are computed from 10 realizations per time bin. Assuming a fraction $f_{\rm acc}$ of a stellar mass m is accreted upon loss-cone entry, the mass accretion rate per unit star is $d\dot{M}^{(\rm A)}_{\rm SMBH}/dN_{\rm A} = f_{\rm acc}\, m\, d\Gamma^{(\rm A)}_{\rm lc}(t|M_{\rm SMBH})/dN_{\rm A}$ where A is the stellar class. We adopt $f_{\rm acc} = 0.5$ for MS stars (TDEs), $f_{\rm acc} = 0.5$ for giants (envelope disruption), and $f_{\rm acc} = 1$ for compact remnants (BHs, NSs, WDs).

During the first $\sim$100 Myr, growth is dominated by MS stars, peaking at $\sim 10^{-2}\,M_\odot\,{\rm yr}^{-1}$ and initially driven by stars $\gtrsim 10\,M_\odot$. At later times ($t \gtrsim 100$ Myr), massive stars evolve into remnants and the disrupted MS population shifts to $\lesssim 10\,M_\odot$. Despite their larger loss cones, giants contribute $\sim$2.5 orders of magnitude less mass than MS stars due to short lifetimes and limited envelope masses, becoming negligible at late times.

MS and giant TDEs produce electromagnetic transients. The MS duty cycle (remnant decay time × loss-cone rate) remains $\sim 10^{-4}$, while giants reach $\sim$1% owing to longer decay times, declining below the MS level after several Gyr.

A few Myr after stellar-mass BH formation, the total accretion rate stabilizes at $\sim 10^{-4}\,M_\odot\,{\rm yr}^{-1}$ for a $10^6\,M_\odot$ SMBH and is higher by a factor of a few for $10^7\,M_\odot$. Accretion is dominated by direct plunges, with negligible inspirals. BHs dominate the late-time growth and contribute significantly even at early times due to mass segregation and their higher masses. WD accretion builds up over several Gyr to just below the MS contribution, while NSs maintain an approximately constant rate of $\sim 5 \times 10^{-6}\,M_\odot\,{\rm yr}^{-1}$ after $\sim$10–100 Myr. Naked cores are negligible because of their short lifetimes and small radii.

Integrating $\dot{M}_{\rm SMBH}$ over $t \in [0, 1]$ Gyr yields total mass growths of $\simeq$3.9, 0.45, and 0.057 times the initial SMBH mass for 10^5, 10^6, and $10^7\,M_\odot$, respectively. The cumulative growth scales approximately as $\propto\sqrt{t}$ (also see N. C. Stone et al. 2017). These values represent upper limits, as relaxation-driven ejections are neglected.

5. Flaring Events

The SMBH disrupts MS stars, while giant-star TDEs are typically partial and involve only envelope stripping (N. N. Navarro & T. Piran 2025). The characteristic flare timescale is the fallback time (S. Gezari 2021, Equation (4)),

$$t_0 \simeq 40\ {\rm days}\ \frac{1\,M_\odot}{m_\star}\left(\frac{R_\star}{R_\odot}\right)^{3/2} \times \left(\frac{M_{\rm SMBH}}{10^6\,M_\odot}\right)^{1/2}, \tag{2}$$

corresponding to the orbital period of the most bound debris. We adopt the shock-powered emission model of J. Krolik et al. (2025), in which stream self-intersections near the apocenter produce radiation with efficiency (J. Krolik et al. 2025, Equation (10))

$$\eta \simeq 4.5 \times 10^{-4}\left(\frac{M_{\rm SMBH}}{10^6\,M_\odot}\right)^{1/3} \times \left(\frac{m_\star}{1\,M_\odot}\right)^{2/3}\frac{R_\odot}{R_\star}. \tag{3}$$

A complete predictive theory of TDE emission remains uncertain (e.g., A. Mummery et al. 2025).

Owing to their large radii, giant-star TDEs produce longer, dimmer flares; we therefore restrict our analysis to MS TDEs. Dense cores, naked cores, and WDs can only be disrupted by intermediate-mass BHs (K. Maguire et al. 2020).

In the efficient-cooling limit ($t_{\rm cool} \ll t_0$), the peak luminosity equals the dissipation rate (J. Krolik et al. 2025, Equation (16)),

$$L_{\rm pk} \simeq 7.8 \times 10^{43}\ {\rm erg\ s^{-1}}\left(\frac{\eta}{4.5 \times 10^{-4}}\right) \times \frac{m_\star}{1\,M_\odot}\frac{40\,d}{t_0}, \tag{4}$$

well below $L_{\rm Edd} \simeq 1.2 \times 10^{45}\,{\rm erg\ s^{-1}}(M_{\rm SMBH}/10^6\,M_\odot)$. For inefficient cooling ($t_{\rm cool} \gg t_0$), $L_{\rm pk} \sim L_{\rm Edd}$ and the flare duration is $t_0 \simeq m_\star c^2/L_{\rm pk}$ (J. Krolik et al. 2025, Equation (18)).

Figure 2 shows the peak luminosities and rest-frame decay times of MS TDEs in the efficient-cooling limit, colored by

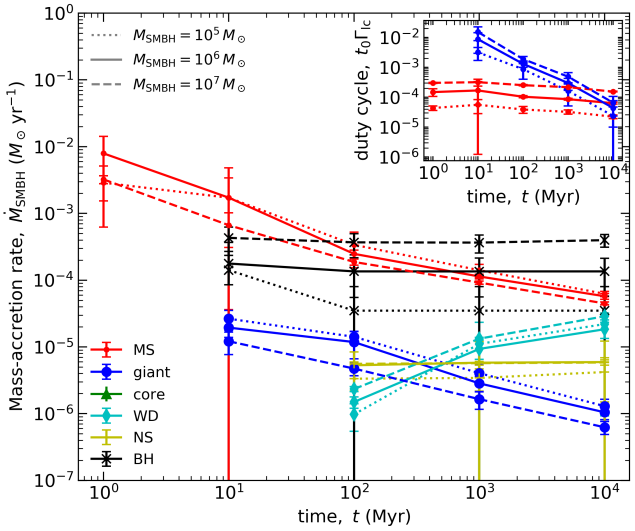

Figure 1. Temporal mass accretion rates from captures onto 10^5 (dotted), 10^6 (solid), and $10^7\,M_\odot$ (dashed) SMBHs, decomposed by stellar type via loss-cone contributions. Abbreviations: MS (main sequence); WD (white dwarf); NS (neutron star); BH (black hole). Points with error bars indicate mean values and standard deviations from 10 realizations. The inset displays the duty cycle of MS (red) and giant (blue) stars.

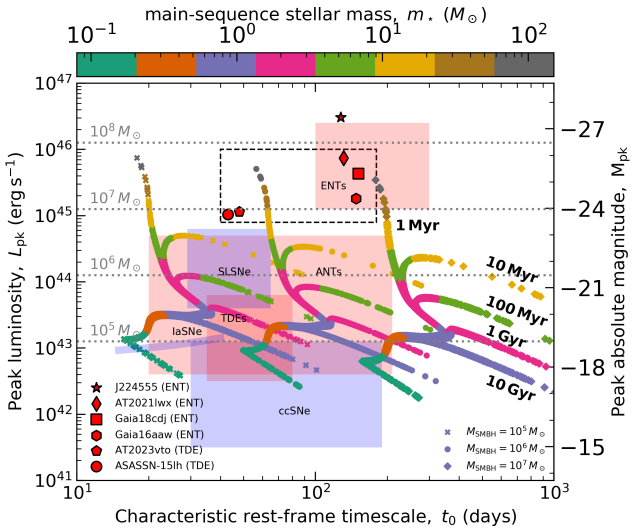

Figure 2. Peak luminosity versus characteristic rest-frame timescale of astronomical transients, with peak absolute magnitudes normalized to a solar V-band magnitude of 4.83; $M_{\rm pk} = 2.5\log_{10}(L_{\rm pk}/L_\odot) - 4.83$. Tidal disruption flares of MS stars by SMBHs of 10^5 (crosses), 10^6 (circles), and $10^7\,M_\odot$ (diamonds) are shown as colored symbols, with the color bar indicating stellar mass. Five distinct sets correspond to five evolutionary times (bold labels). The six red symbols denote observed flares with $L_{\rm pk} > 10^{45}$ erg s^{-1}. Gray dotted horizontal lines mark the Eddington luminosities for the labeled SMBH masses. Abbreviations: ENTs (extreme nuclear transients); SLSNe (superluminous supernovae); ANTs (ambiguous nuclear transients); TDEs (tidal disruption events); ccSNe (core-collapse supernovae); Ia SNe (Type Ia supernovae) following the Phillips relationship.

stellar mass, alongside observed transient classes and six extreme flares (M. J. Graham et al. 2026; J. T. Hinkle et al. 2025). The most luminous events arise from the most massive MS stars. As the stellar population evolves, the maximum MS mass decreases while stellar radii increase near turnoff, producing a late-time turnover since $t_0 \propto R_\star^{3/2}$. TDEs of $\sim$30–150 $M_\odot$ MS stars by 10^6–$10^7\,M_\odot$ SMBHs are consistent with ENTs, while lower-mass systems fall in the ANT regime.

6. Integration over Cosmological Volume

We focus on the redshift range $z < 6$. Assuming a constant SMBH mass function with comoving number density $n_{\rm SMBH}$, we weight three representative SMBH masses by $w_j \propto M_{{\rm SMBH},j}^{-2}$ and normalize $\sum_j w_j = 1$. Our choice of equal SMBH mass per unit logarithmic SMBH mass bin in the examined mass range is motivated by E. Gallo & A. Sesana (2019) and J. E. Greene et al. (2020). The source-frame loss-cone rate density for class A is

$$\mathcal{R}_{\rm lc}^{(\rm A)} \simeq \frac{n_{\rm SMBH}}{10^{-2}\,{\rm Mpc}^{-3}} \sum_{k=1}^{5}\sum_{j=1}^{3} w_j \frac{\Gamma_{\rm lc}^{(\rm A)}(t_k|M_{{\rm SMBH},j})}{10^{-5}\,{\rm yr}^{-1}} \times 20\,{\rm Gpc}^{-3}\,{\rm yr}^{-1}, \quad (5)$$

including both captures and inspirals, and assuming a uniform time prior over which index $\boldsymbol{k}$ runs.

The observer-frame rate follows from integrating over comoving volume and applying cosmological time dilation (K. Kritos & J. Silk 2025, Equation (27)). Assuming $\mathcal{R}_{\rm lc}^{(\rm A)}$ is constant over $0 \leqslant z \leqslant 6$,

$$R_{\rm lc}^{(\rm A)} \simeq \frac{\mathcal{R}_{\rm lc}^{(\rm A)}}{20\,{\rm Gpc}^{-3}\,{\rm yr}^{-1}} \frac{\int_{z=0}^{z=6}(1+z)^{-1}dV_{\rm com}(z)}{6.9\times10^{11}\,{\rm Mpc}^3} \times 1.4\times10^4\,{\rm yr}^{-1}, \quad (6)$$

scaling linearly with $n_{\rm SMBH}$. Rates are summarized in Table 1.

Table 1
Capture and Inspiral Loss-cone Density and Volume-integrated Rates over $0 \leqslant z \leqslant 6$ for Different Stellar Classes

A	$\mathcal{R}_{\rm capture}$ (Gpc^{-3} yr^{-1})	$R_{\rm capture}$ (yr^{-1})	$\mathcal{R}_{\rm inspiral}$ (Gpc^{-3} yr^{-1})	$R_{\rm inspiral}$ (yr^{-1})
MS	5.4×10^3	3.8×10^6	4.7×10^{-6}	4.4×10^{-2}
giant	1.5×10^2	1.1×10^5	1.6×10^{-7}	3.3×10^{-3}
WD	8.6×10^1	6.0×10^4	4.9×10^{-8}	1.5×10^{-3}
NS	1.5×10^1	1.0×10^4	1.1×10^{-10}	9.9×10^{-7}
BH	2.2×10^1	1.5×10^4	2.8×10^{-7}	1.9×10^{-2}

The total SMBH mass growth over $z \in [0, 6]$ is

$$\approx \frac{n_{\rm SMBH}}{10^{-2}\,{\rm Mpc}^{-3}} \sum_{j=1}^{3} w_j \frac{\int_0^{10\,{\rm Gyr}} dt\,\dot{M}_{{\rm SMBH},j}(t)}{1.8\times10^6\,M_\odot} \times 1.8\cdot10^{13}\,M_\odot\,{\rm Gpc}^{-3}, \quad (7)$$

which is on the same order as Sołtan's estimated mass density ($8\times10^{13}\,M_\odot\,{\rm Gpc}^{-3}$; A. Soltan 1982), implying gas accretion dominates SMBH growth but loss-cone effects contribute at the $\sim$25% level.

We find an MS TDE rate of $\approx 5\times10^3\,{\rm Gpc}^{-3}\,{\rm yr}^{-1}$ at $4 \leqslant z \leqslant 6$, with only a small detectable fraction (e.g., UVEX; S. R. Kulkarni et al. 2021), while inspirals are negligible in all classes. For comparison, the local TDE rate density is $\sim$15–200 $\,{\rm Gpc}^{-3}\,{\rm yr}^{-1}$ (S. van Velzen & G. R. Farrar 2014), below theoretical $z \sim 0$ expectations (N. C. Stone & B. D. Metzger 2016), while recent candidates at $z > 1$ (Y. Gu et al. 2025) imply rates of $\sim$20–80 $\,{\rm Gpc}^{-3}\,{\rm yr}^{-1}$ at $z \sim 1$ (M. J. Graham et al. 2026). In addition, $\mathcal{R}_{\rm MS}$: $\mathcal{R}_{\rm giant} \sim 30$. Finally, stellar remnants capture at intrinsic

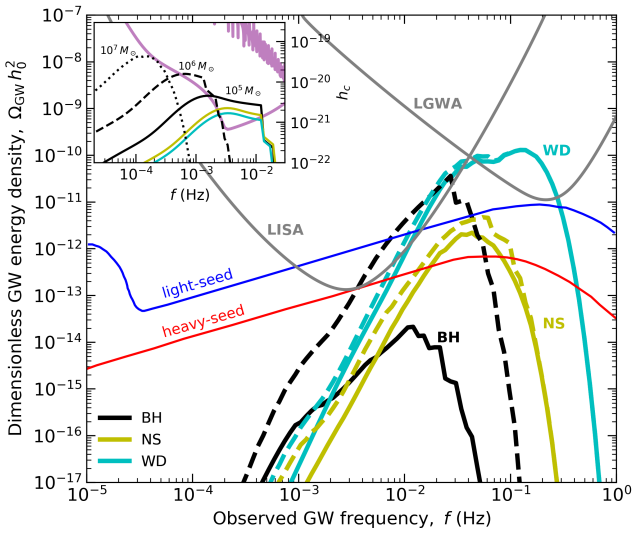

Figure 3. Total dimensionless gravitational-wave (GW) energy density from BH (black), NS (yellow), and WD (cyan) captures within $z < 6$ as a function of the observed GW frequency. The comoving SMBH number density is assumed constant at 10^{-2} Mpc^{-3}. Gray curves indicate the PLS of LISA and LGWA with an SNR = 10 and $T_{\rm obs} = 4$ yr. Also shown are the GW backgrounds from mergers of massive BHs under the light- and heavy-seed scenarios (M. Çalışkan et al. 2025). The inset shows the characteristic strain for a few $z \sim 5$ captures.

rates of hundreds per year, and about two BH-EMRIs every century, producing GW sources, which we discuss next.

7. Gravitational-wave Background

We compute the characteristic GW strain of each capture, $h_c(f)$, at the observer-frame frequency f, using Equation (17) of M. Bonetti & A. Sesana (2020), including the first 100 harmonics. Merger-ringdown and spin effects are neglected. Example individual sources at $z \sim 5$ are shown in the inset of Figure 3 together with the sensitivities of LGWA (J. Harms et al. 2021) and LISA (P. Amaro-Seoane et al. 2017). Captures originate from highly eccentric ($e \simeq 1^-$) orbits that rapidly circularize and merge within$\simeq$28 min $M_{\rm SMBH}/(10^6\,M_\odot)(10\ {\rm km\ s^{-1}}/\sigma)^3$(R.M.O'Leary et al. 2009). We find that $\simeq$54% ($\simeq$1.3%), $\simeq$7.9% ($\simeq$0.6%), and $\simeq$3.3% ($\simeq$0.5%) of all BH, NS, and WD captures, respectively, have signal-to-noise ratio (SNR) > 10 in LISA (LGWA).

The cumulative contribution of captures produces a stochastic GW background (SGWB), whose dimensional energy density over an observation time $T_{\rm obs}$ we approximate as (E. Belgacem et al. 2025, Equation (3.83))

$$\Omega_{\rm lc}^{(\rm A)}(f)h_0^2 = \frac{1\ {\rm yr}}{T_{\rm obs}}\left(\frac{f}{10^{-2}\ {\rm Hz}}\right)^3 \times \sum_{i=1}^{\tilde{\mathcal{N}}_{\rm A}}\sum_{j=1}^{3} w_j \left[\frac{h_{c,ij}(f)}{10^{-20}}\right]^2 \times 2\cdot 10^{-13}\,\frac{\tilde{\mathcal{N}}_{\rm A}}{10^4}, \quad (8)$$

where A = {WD, NS, BH} and h_0 is the reduced Hubble's constant. The sum is over undetectable $\tilde{\mathcal{N}}_{\rm A}$ captures with SNR < 10, by convention.

The resulting SGWBs are shown in Figure 3 (thick lines). The WD capture background peaks at dHz and are observable with an SNR > 10 when compared with the corresponding LGWA Power-Law integrated Sensitivity (PLS; P. Ajith et al. 2025) and LISA PLS (K. Schmitz 2020) for $T_{\rm obs} = 4$ yr. For comparison, we also show the background from massive BH mergers under two seeding scenarios (M. Çalışkan et al. 2025). While the BH and NS backgrounds have SNR < 10 within 4 yr, there are still thousands of captures within $z < 6$ with LISA. Finally, the SGWB from inspirals is undetectable.

8. Formation of the Black Hole Star

We adopt a BH-star framework in which the SMBH is embedded in a dense cocoon of gas and stars. This model satisfies spectral constraints on LRDs and enables rapid SMBH growth via bursty, super-Eddington gas accretion (V. Kokorev et al. 2025; K. Kritos & J. Silk 2025). The buildup of dense gas cocoons produces extreme Balmer breaks, Balmer absorption, and Hβ emission, and resembles the phenomenon of BH stars (A. de Graaff et al. 2025; R. P. Naidu et al. 2025; see also D. Nandal & A. Loeb 2026; V. Rusakov et al. 2025; M. C. Begelman & J. Dexter 2026).

Feedback-regulated growth yields universal scalings: momentum conservation gives $M_{\rm BH} \propto \sigma^4$,

$$f_{\rm Edd}\left(\frac{4\pi G M_{\rm SMBH} c}{\kappa_{\rm es}}\right) = \frac{\epsilon\sigma^4 v_s}{G}, \quad (9)$$

while energy conservation implies $M_{\rm SMBH} \propto \sigma^5$. The SMBH radius of influence, $r_{\rm infl} \sim$ 10–30 pc, defines the Bondi radius.

Accretion-disk sizes inferred from reverberation mapping are typically parsec scale. The Eddington feedback region is set by requiring a unit Thomson optical depth,

$$(n_e\sigma_T)^{-1} = m_p M_g^2 G^3 \sigma^{-6}\sigma_T^{-1} \simeq (M_g/M_\odot)^2\,\sigma_{200}^{-6}, \quad (10)$$

using $\rho_g = \sigma^6 G^{-3} M_g^{-2}$ and stellar-mass form factors (P. Diener et al. 1995). This defines a dense central core at radii $\sim$1–10 au, consistent with CLOUDY models of inverted LRD spectra and inferred gas densities $n_{\rm H} \sim 10^8\,{\rm cm^{-3}}$ (A. J. Taylor et al. 2025).

Observations and theory favor Comptonization-regulated feedback (R. Gilli et al. 2022): momentum-driven regulation dominates at high redshift, while energy-driven feedback with momentum boosting becomes important at low redshift, enhancing early star formation and later driving massive outflows (T. Costa et al. 2014; J. Silk et al. 2024).

9. Conclusions

We modeled stellar feeding onto SMBHs in NSCs, including TDEs and compact-object captures. Stellar plunges contribute only a sizable fraction to SMBH mass growth; however, gas accretion still dominates at all redshifts.

Main-sequence TDEs dominate the electromagnetic output. Disruptions of massive ($\sim$30–150 $M_\odot$) stars by 10^6–$10^7\,M_\odot$ SMBHs naturally reproduce the luminosities and timescales of ENTs, while giant-star TDEs are negligible. We predict an intrinsic MS TDE rate of $\sim 5\times10^3\,{\rm Gpc^{-3}\,yr^{-1}}$ at $4 \leqslant z \leqslant 6$. A fraction of these are expected to be observed with the LSST (M. Karmen et al. 2026).

Compact-object captures produce thousands of detectable LISA sources within $z < 6$ and generate a stochastic GW background, dominated by WD captures at dHz frequencies.

Stellar feeding is therefore an inevitable byproduct of dense, rapidly growing high-redshift nuclei; insufficient for SMBH growth, but observable through extreme TDEs and GWs, providing a direct probe of BH-star systems and early SMBH assembly.

Our data and code are publicly available on Zenodo: DOI:10.5281/zenodo.18471816

Acknowledgments

We thank Mesut Çaliskan, Marco Chiaberge, Muryel Guolo, Francesco Iacovelli, Mitchell Karmen, Julian Krolik, Colin Norman, David Pereñiguez, and the anonymous referee for discussions and comments. K.K. is supported by NSF grant Nos. AST-2307146, PHY-2513337, PHY-090003, and PHY-20043, by NASA grant No. 21-ATP21-0010, by John Templeton Foundation grant No. 62840, by the Simons Foundation [MPS-SIP-00001698, E.B.], by the Simons Foundation International, by Italian Ministry of Foreign Affairs and International Cooperation grant No. PGR01167, and by the Onassis Foundation Scholarship (ID: F ZT 041-1/2023-2024).

Appendix
Extended Tables of Loss-cone Rates

This Appendix presents capture loss-cone rates and associated uncertainties for each stellar type at the five different epochs onto a 10^5 (Table 2), 10^6 (Table 3), and $10^7\,M_\odot$ (Table 4) SMBH.

Table 2
Capture Loss-cone Rates onto $M_{\rm SMBH} = 10^5\,M_\odot$ in $\rm yr^{-1}$ at Evolution Time t for Different Stellar Types

Stellar Type	t				
	1 (Myr)	10 (Myr)	100 (Myr)	1000 (Myr)	10,000 (Myr)
MS	$(6.7 \pm 1.2) \times 10^{-4}$	$(7 \pm 2) \times 10^{-4}$	$(5.3 \pm 1.0) \times 10^{-4}$	$(4.3 \pm 0.5) \times 10^{-4}$	$(3.4 \pm 0.6) \times 10^{-4}$
giant	0	$(2.0 \pm 1.3) \times 10^{-5}$	$(1.8 \pm 0.3) \times 10^{-5}$	$(3.1 \pm 1.2) \times 10^{-5}$	$(6.7 \pm 1.3) \times 10^{-6}$
WD	0	0	$(8 \pm 4) \times 10^{-7}$	$(1.3 \pm 1.3) \times 10^{-5}$	$(3 \pm 2) \times 10^{-5}$
NS	0	0	$(2.2 \pm 0.7) \times 10^{-6}$	$(2.3 \pm 0.8) \times 10^{-6}$	$(3 \pm 2) \times 10^{-6}$
BH	0	$(5.2 \pm 0.7) \times 10^{-6}$	$(1.9 \pm 1.8) \times 10^{-6}$	$(1.9 \pm 1.8) \times 10^{-6}$	$(1.9 \pm 1.8) \times 10^{-6}$

Note. Rates of naked cores are zero. Error bars are standard deviations estimated over 10 realizations. Total number of stellar objects within the influence radius is $N_\star = 301, 550$. Abbreviations: MS (main sequence); WD (white dwarf); NS (neutron star); BH (black hole).

Table 3
Same as Table 2 with $M_{\rm SMBH} = 10^6\,M_\odot$

Stellar Type	t				
	1 (Myr)	10 (Myr)	100 (Myr)	1000 (Myr)	10,000 (Myr)
MS	$(8 \pm 3) \times 10^{-4}$	$(6 \pm 4) \times 10^{-4}$	$(3.8 \pm 0.2) \times 10^{-4}$	$(3.8 \pm 0.2) \times 10^{-4}$	$(2.4 \pm 0.2) \times 10^{-4}$
giant	0	$(0.5 \pm 0.5) \times 10^{-5}$	$(1.4 \pm 0.2) \times 10^{-5}$	$(2.0 \pm 1.3) \times 10^{-5}$	$(5.3 \pm 1.0) \times 10^{-6}$
WD	0	0	$(1.2 \pm 0.2) \times 10^{-6}$	$(1.0 \pm 0.3) \times 10^{-5}$	$(2.6 \pm 0.6) \times 10^{-5}$
NS	0	0	$(4 \pm 2) \times 10^{-6}$	$(3 \pm 2) \times 10^{-6}$	$(3 \pm 2) \times 10^{-6}$
BH	0	$(9 \pm 4) \times 10^{-6}$	$(1.1 \pm 0.7) \times 10^{-5}$	$(1.1 \pm 0.7) \times 10^{-5}$	$(1.1 \pm 0.7) \times 10^{-5}$

Note. Total number of stellar objects within the influence radius is $N_\star = 3, 015, 502$.

Table 4
Same as Table 2 with $M_{\rm SMBH} = 10^7\,M_\odot$

Stellar Type	t				
	1 (Myr)	10 (Myr)	100 (Myr)	1000 (Myr)	10,000 (Myr)
MS	$(4.9 \pm 0.2) \times 10^{-4}$	$(4.3 \pm 0.4) \times 10^{-4}$	$(3.5 \pm 0.2) \times 10^{-4}$	$(3.0 \pm 0.1) \times 10^{-4}$	$(2.29 \pm 0.06) \times 10^{-4}$
giant	0	$(1.0 \pm 0.4) \times 10^{-5}$	$(7.4 \pm 1.6) \times 10^{-6}$	$(1.2 \pm 0.1) \times 10^{-5}$	$(3.2 \pm 0.6) \times 10^{-6}$
WD	0	0	$(1.9 \pm 0.2) \times 10^{-6}$	$(1.49 \pm 0.07) \times 10^{-5}$	$(4.2 \pm 0.3) \times 10^{-5}$
NS	0	0	$(3.8 \pm 0.2) \times 10^{-6}$	$(3.8 \pm 0.2) \times 10^{-6}$	$(3.9 \pm 0.4) \times 10^{-6}$
BH	0	$(1.7 \pm 0.6) \times 10^{-5}$	$(1.9 \pm 0.7) \times 10^{-5}$	$(1.8 \pm 0.5) \times 10^{-5}$	$(2.0 \pm 0.3) \times 10^{-5}$

Note. Total number of stellar objects within the influence radius is $N_\star = 30, 155, 026$.

ORCID iDs

Konstantinos Kritos https://orcid.org/0000-0002-0212-3472
Joseph Silk https://orcid.org/0000-0002-1566-8148

References

Ajith, P., Seoane, P. A., Arca Sedda, M., et al. 2025, JCAP, 01, 108
Alexander, T., & Hopman, C. 2003, ApJL, 590, L29
Amaro-Seoane, P., Audley, H., Babak, S., et al. 2017, arXiv:1702.00786
Banerjee, S., Belczynski, K., Fryer, C. L., et al. 2020, A&A, 639, A41
Belgacem, E., Iacovelli, F., Maggiore, M., Mancarella, M., & Muttoni, N. 2025, JCAP, 04, 032
Begelman, M. C., & Dexter, J. 2026, ApJ, 996, 48
Bellovary, J. 2025, ApJL, 984, L55
Bonetti, M., & Sesana, A. 2020, PhRvD, 102, 103023
Çalışkan, M., Anil Kumar, N., Kamionkowski, M., & Cheng, S. 2025, arXiv:2506.18965
Costa, T., Sijacki, D., & Haehnelt, M. G. 2014, MNRAS, 444, 2355
de Graaff, A., Rix, H.-W., Naidu, R. P., et al. 2025, A&A, 701, A168
Diener, P., Kosovichev, A. G., Kotok, E. V., Novikov, I. D., & Pethick, C. J. 1995, MNRAS, 275, 498
Evans, C. R., & Kochanek, C. S. 1989, ApJL, 346, L13
Frank, J., & Rees, M. J. 1976, MNRAS, 176, 633
Frederick, S., Gezari, S., Graham, M. J., et al. 2021, ApJ, 920, 56
Gallo, E., & Sesana, A. 2019, ApJL, 883, L18
Gezari, S. 2021, ARA&A, 59, 21
Gilli, R., Norman, C., Calura, F., et al. 2022, A&A, 666, A17
Graham, M. J., McKernan, B., Ford, K. E. S., et al. 2026, NatAs, 10, 154
Greene, J. E., Strader, J., & Ho, L. C. 2020, ARA&A, 58, 257
Greene, J. E., Labbe, I., Goulding, A. D., et al. 2024, ApJ, 964, 39
Gu, Y., Zhang, X.-G., Chen, X.-Q., Yang, X., & Liang, E.-W. 2025, MNRAS, 537, 84
Gurkan, M. A., & Hopman, C. 2007, MNRAS, 379, 1083
Harms, J., Ambrosino, F., Angelini, L., et al. 2021, ApJ, 910, 1
Hinkle, J. T., Shappee, B. J., Auchettl, K., et al. 2025, SciA, 11, eadt0074
Hopman, C., & Alexander, T. 2006a, ApJ, 645, 1152
Hopman, C., & Alexander, T. 2006b, ApJL, 645, L133
Juodžbalis, I., Marconcini, C., D'Eugenio, F., et al. 2025, arXiv:2508.21748
Karmen, M., Gezari, S., Norman, C., & Guolo, M. 2026, arXiv:2602.04947
Kokorev, V., Chisholm, J., Naidu, R. P., et al. 2025, arXiv:2511.07515
Kritos, K., & Silk, J. 2025, arXiv:2510.21709
Krolik, J., Piran, T., & Ryu, T. 2025, ApJ, 988, 220
Kulkarni, S. R., Harrison, F. A., Grefenstette, B. W., et al. 2021, arXiv:2111.15608
Maguire, K., Eracleous, M., Jonker, P. G., MacLeod, M., & Rosswog, S. 2020, SSRv, 216, 39
Maiolino, R., Scholtz, J., Curtis-Lake, E., et al. 2024, A&A, 691, A145
Mandel, I. 2021, RNAAS, 5, 223
Matthee, J., Naidu, R. P., Brammer, G., et al. 2024, ApJ, 963, 129
McConnell, N. J., Ma, C.-P., Gebhardt, K., et al. 2011, Natur, 480, 215
Melchor, D., Naoz, S., Gezari, S., & Mockler, B. 2025, ApJL, 992, L21
Merritt, D. 2013, Dynamics and Evolution of Galactic Nuclei (Princeton Univ. Press)
Mummery, A. 2024, MNRAS, 527, 6233
Mummery, A., Metzger, B., van Velzen, S., & Guolo, M. 2025, arXiv:2512.09143
Naidu, R. P., Matthee, J., Katz, H., et al. 2025, arXiv:2503.16596
Nandal, D., & Loeb, A. 2026, ApJ, 998, 124
Navarro, N. N., & Piran, T. 2025, ApJ, 983, 177
O'Leary, R. M., Kocsis, B., & Loeb, A. 2009, MNRAS, 395, 2127
Quinlan, G. D., & Shapiro, S. L. 1989, ApJ, 343, 725
Rauch, K. P., & Tremaine, S. 1996, NewA, 1, 149
Rusakov, V., Watson, D., Nikopoulos, G. P., et al. 2025, Natur, 649, 574
Schmitz, K. 2020, Symm, 12, 1477
Silk, J., Begelman, M. C., Norman, C., Nusser, A., & Wyse, R. F. G. 2024, ApJ, 961, L39
Soltan, A. 1982, MNRAS, 200, 115
Stone, N. C., Küpper, A. H. W., & Ostriker, J. P. 2017, MNRAS, 467, 4180
Stone, N. C., & Metzger, B. D. 2016, MNRAS, 455, 859
Syer, D., & Ulmer, A. 1999, MNRAS, 306, 35
Taylor, A. J., Kokorev, V., Kocevski, D. D., et al. 2025, ApJL, 989, L7
van Velzen, S., & Farrar, G. R. 2014, ApJ, 792, 53
van Velzen, S., Holoien, T. W. S., Onori, F., Hung, T., & Arcavi, I. 2020, SSRv, 216, 124
Wiseman, P., Williams, R. D., Arcavi, I., et al. 2025, MNRAS, 537, 2024